Journal of Metals, Materials and Minerals, 34(4), 1982, 2024

Surface characteristics evolution of 316L stainless steel induced by tension loading

Kanokwan ANTANAM[1], Surasak KUIMALEE[2], Panya BUAHOMBURA[1], and Waraporn PIYAWIT[1,*]

[1] *Suranaree University of Technology, School of Metallurgical Engineering, Institute of Engineering, Nakhon Ratchasima, 30000, Thailand*
[2] *Maejo University, Industrial Chemistry Innovation Programme, Faculty of Science, Chiang Mai, 50290, Thailand*

***Corresponding author e-mail**: wpiyawit@sut.ac.th

Received date:
2 March 2024
Revised date:
7 July 2024
Accepted date:
27 September 2024

Keywords:
316L stainless steel;
Plastic deformation;
Surface relief;
Contact angle;
Surface free energy

Abstract

316L stainless steel has been employed as a medical implant material owing to its advantageous biocompatibility and durability. The microstructure and surface characteristics of 316L play a crucial role in implant application. Diverse processing methods were utilized to modify the surface properties of 316L to customize the characteristics of medical devices. Mechanical deformation induces changes in the microstructure and causes changes in surface topography. In this study, we introduced deformation to 316L by applying uniaxial tension at strain values ranging from 2% to 25%. During sample preparation, electrochemical polishing was employed to eliminate the deformed layers generated by mechanical grinding. After the tensile test, a contact angle test was conducted. The surface relief of 316L was examined using three-dimensional (3D) laser scanning microscopy and atomic force microscopy. X-ray diffraction with CuK radiation in the Bragg–Brentano (θ–θ) mode was also employed to identify the phase transformation. It can be concluded that higher strain levels increased surface roughness and the number of slip lines. At higher strain levels, samples exhibited a martensitic transformation, affecting topography changes and the surface free energy. The contact angle measurement results and surface free energy determination showed improved wettability following plastic deformation. Determining the factors that affect surface wettability requires an understanding of the relationship between surface free energy, topography, and surface roughness. Deformation-induced martensite can significantly increase the surface free energy and wettability of 316L stainless steel (SS) by altering strain levels. It is important to consider surface characteristics to understand slip mechanisms at grain boundaries, particularly in cases where surfaces have been electropolished. Nevertheless, the surface also manifested deformation-induced martensitic (DIM) transformation, potentially posing a risk to the passive film and contributing to corrosion, consequently reducing the implant's lifespan.

1. Introduction

316L stainless steel is an austenitic alloy with a chromium content of 16% to 18%, nickel content of 10% to12%, a maximum carbon level of 0.03%, and a molybdenum value of 2% to 3%. Possessing superior properties such as biocompatibility, mechanical strength, toughness, formability, and corrosion resistance across diverse environments (including chemical, pitting, crevice corrosion, and oxidation resistance), 316L is well-suited for applications in temporary orthopedic devices and bone fixation implants. Fixation devices stabilize fractured bones and other tissues during the natural healing process.

The surface characteristics of 316L stainless steel significantly influence its performance as an implant, with surface roughness being a key determinant. Surface roughness typically ranges from below 0.1 μm to several micrometers for fixation implants. Variances in surface topography at different roughness levels impact cell attachment, growth, bacterial adhesion, and biofilm formation. The surface roughness of implants plays a pivotal role in bone tissue anchoring, wherein rougher surfaces improve cell adhesion and tissue development, albeit potentially compromising implant stability [1].

In orthopedic implants, the study of biomaterial–cell interactions has focused on evaluating surface wettability through contact angle differentiation. The contact angle between a substrate and a liquid can be used to determine wettability. Interpreting the solid's surface free energy is one of the most significant applications of contact angle measurement. This energy can be calculated using Owen and Wendt's continued Fowkes (OWRK) techniques, equating it to the surface tension of a liquid measured in the same unit ($mN{\cdot}m^{-1}$) [2]. The 316L stainless steel implant wettability enhancement can be achieved through surface chemistry, surface roughness, or surface topography modifications.

Hence, surface topography and roughness characteristics are crucial parameters in material selection. Diverse manufacturing techniques exist to augment implant surface roughness, with surface and bulk modification methods employed to enhance stainless steel implants' biointegration and mechanical strength. However, mechanical treatments such as tension and compression may induce modifications in the material's microstructure and mechanical properties, resulting in plastic deformation. While these alterations can impact implant performance, their interaction with the environment is controlled by the properties of their surface layers.

Plastic deformation significantly enhances surface wettability, improves cell responsiveness, and facilitates tissue–implant integration [3]. Various plastic deformation schemes can effectively modify the surface roughness, surface free energy, and wettability of 316L stainless steel. However, a comprehensive understanding of microstructural changes during plastic deformation and specific insights into surface topography evolution through deformation remain elusive.

The 316L austenitic stainless steel, characterized by low stacking fault energy, undergoes deformation through twinning and slip mechanisms. Additionally, the deformation process can induce martensite formation or deformation-induced martensitic transformation (DIM), with DIM increasing proportionally to the degree of deformation. Amplification of DIM phases may destroy the 316L passive film, which is crucial for the material's biocompatibility and corrosion resistance. Damage to the passive film could expose the metal underneath to corrosive conditions, potentially impacting the implant's performance and shortening its longevity.

In our recent study, we aim to elucidate the relationship between surface conditions and the wettability of 316L stainless steel. To investigate this phenomenon, tested samples underwent varying degrees of elongation under uniaxial force. The evolution of surface topography in relation to the degree of deformation will be presented through various microscopy techniques, including atomic force microscopy (AFM), 3D laser scanning microscopy, and optical microscopy. Phase transformation was investigated using an X-ray diffractometer and nanoindentation. Contact angle measurements were also performed to assess wettability characteristics and measure surface free energy. This information is vital for gaining deeper insights into the role of surface characteristics in the biocompatibility of implants. This research expands upon previous studies that emphasize the importance of plastic deformation in influencing surface properties. At different strain levels, plastic deformation can lead to varying results in the surface topography of a material, along with its surface free energy.

2. Experimental procedures

2.1 Materials

A sheet of austenitic 316L stainless steel is 2 mm thick, characterized by a chemical composition of 0.02 C, 2.02 Mo, 10.09 Ni, 0.029 P, 16.76 Cr, 0.06 N, 0.46 Si, 0.027 S, 1.77 Mn, and balanced Fe, was employed in this uniaxial tension loading experiment. The tensile samples, prepared according to ASTM E8, were laser-cut into sub-sized dog bone shapes. Figure 1 shows a schematic representation of the tested sample.

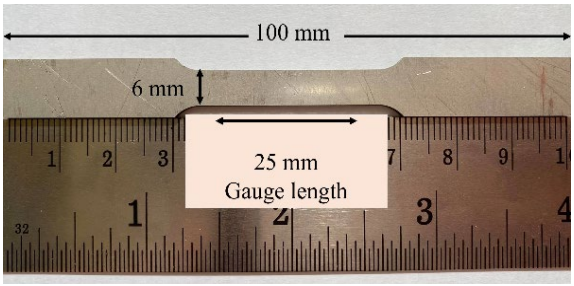

Figure 1. Schematic of the tensile testing sample according to ASTM E8.

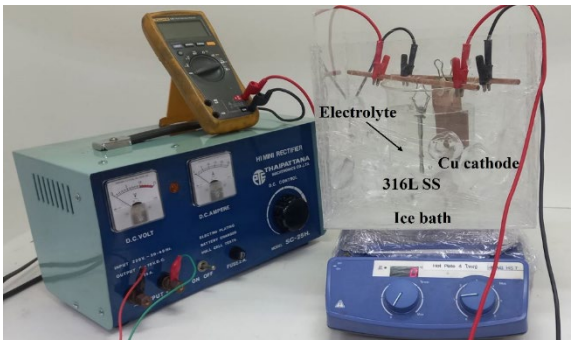

Figure 2. Electrolytic polishing experimental setup with a cooling bath.

Table 1. Electrolytic polishing parameters.

Current (A)	Voltage (V)	Current density ($A \cdot mm^{-2}$)	Temperature (°C)	Time (min)
0.20	3	0.02	15	15

2.2. Sample preparation

The tested samples underwent mechanical grinding and polishing, followed by electrolytic polishing to remove the deformed layer from the surface. The electrolytic polishing solution comprised 40% v/v sulfuric acid (H_2SO_4) and 60% v/v phosphoric acid (H_3PO_4). A copper cathode plate was positioned 30 mm from the anode. The parameters for the electrolytic polishing process are listed in Table 1. To maintain the electrolyte temperature at 15°C, the electrochemical cell was placed in a cooling bath filled with ice, as shown in Figure 2. After electro-polishing, the samples underwent a 15 min ultrasonic cleaning in ethanol, followed by drying in an ambient environment.

2.3 Mechanical deformation under uniaxial tension

The universal testing machine (Instron 5569 Model, Norwood, MA, USA) equipped with a maximum testing force of 50 kN, was employed for the tension loading of dog bone-shaped samples at room temperature. The testing was conducted at a constant crosshead speed of 0.5 $mm \cdot min^{-1}$. Following ASTM E8 guidelines, each sample was evaluated with a traveling crosshead interrupted at 12, 25, 45, and 100 $mm \cdot mm^{-1}$ tensile strains, inducing deformations at 2%, 5%, 10%, and 25% strains, respectively. The strain value for each deformed sample was determined by comparing the elongated gauge length with the initial gauge length.

2.4 Surface characterization

The area roughness (Ra) measurement was conducted using Laser scanning microscopy (LSM) with a 0.4 μm diameter laser beam, employing an Olympus LEXT OLS5100. AFM was carried out using a Park Systems AFM XE-1 equipped with a single silicon crystal probe and Cr–Co coating, operating in a non-contact mode at a scan rate of 0.22 Hz. X-ray diffraction (XRD) profiles of the 316L sample were obtained using a Bruker D8 Advance instrument with Cu Kα radiation (wavelength of 1.5406 Å), and the investigations were performed at room temperature. The diffraction angles were scanned between 30° and 100° with a scan step size of 0.02° and step time of 0.5 s.

2.5 Contact angle measurement

Contact angle measurement is a technique for evaluating wettability. The sessile drop method was employed to measure the static contact angle at room temperature, utilizing two different testing liquids, water and glycerol. Measurements were taken at the center of the gauge length. To perform contact angle measurements, 316L samples were positioned in the focal point, and a micropipette approached the sample surface until a 10 µL droplet of the test liquid touched the surface. After 60 s, the shape of the liquid droplet on the surface was recorded using a USB digital microscope. The average contact angles and standard deviation for each sample were determined through statistical data analysis based on at least five measurements. Figure 3 shows the contact angle measurement setup on the sample surface.

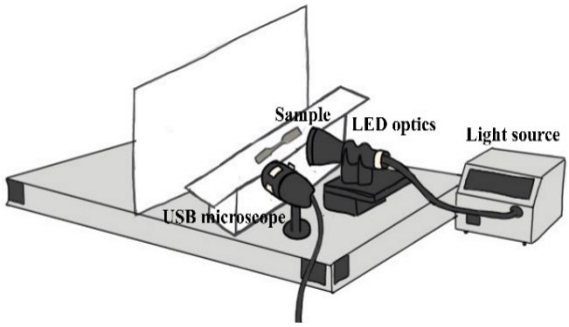

Figure 3. Schematic of the experimental setup for contact angle measurements.

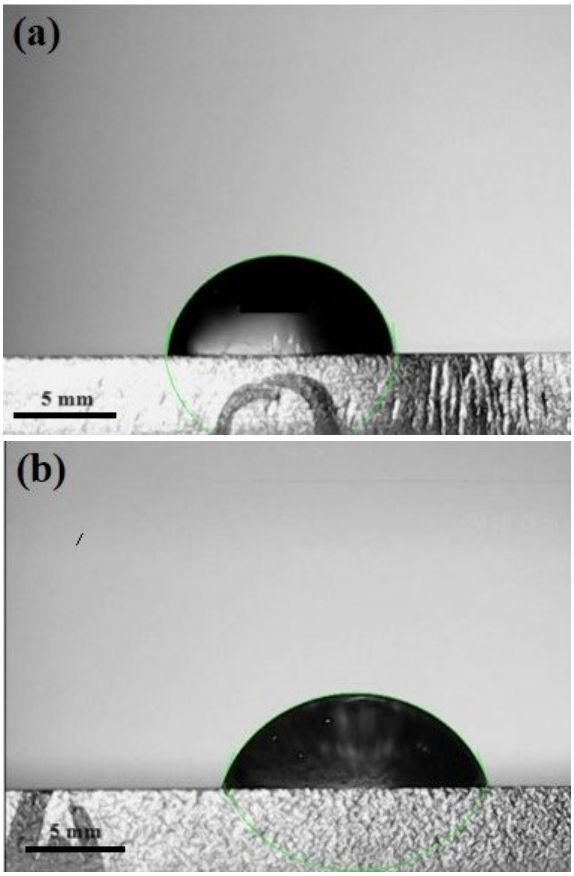

Figure 4. Contact angle of (a) 5% strain and (b) 25% strain samples obtained using the Drop Analysis (LB-ADSA).

2.6 Surface free energy determination

The surface free energy is crucial in determining the wettability of liquid testing on a 316L surface [4]. Surface free energy calculations were performed using the indirect surface tension measurement method. The assessment of surface free energy at different strain levels utilized the Owens–Wendt method modified by Zhang *et al*. [5]. However, water and glycerol were employed for this study instead of diiodomethane owing to its toxicity. The following geometric mean relationship for solid–liquid interfacial surface tension, derived from Equation (1), is obtained by considering the interfacial energy contributed by the polar and dispersive components (γSL).

$$\gamma SL = \gamma S + \gamma L + 2\sqrt{g_S^d g_L^d} - 2\sqrt{g_S^P g_L^P} \quad (1)$$

Where γL is the surface tension of the liquid, liquid polar component (g_L^P), liquid dispersive component (g_L^d), and γS is the surface tension of the solid, solid polar component (g_S^P), and solid dispersive component (g_S^d).

The balance at the three-phase contact of solid–fluid–fluid is governed by Young's equation (Equation (2)), where γSG and γLG represent the interfacial surface tensions of the solid–gas and liquid–gas interfaces. Young's contact angle (θ) is based on the assumption of a smooth and chemically homogeneous surface, which is influenced by the test liquid [6]. Substituting the surface free energy obtained from Equation (1) into Young's Equation leads to the Owens–Wendt contact angle model, as shown in Equation (3).

$$g_{SG} = g_{SL} + g_{LG}\cos\theta \quad (2)$$

$$\frac{g_L(1+\cos\theta)}{2\sqrt{g_L^P}} = \sqrt{\frac{g_L^d}{g_L^P}}\sqrt{g_S^d} + \sqrt{g_S^P} \quad (3)$$

Equation (3) can be reformulated into a linear expression for directly assessing surface energy using $\frac{g_L(1+\cos\theta)}{2\sqrt{g_L^P}}$ as the dependent variable and $\sqrt{\frac{g_L^d}{g_L^P}}$ as the independent variable. The square of the slope in the linearized Owens−Wendt plot is $\sqrt{g_S^d}$, and the square of the intercept is equal to $\sqrt{g_S^P}$. The contact angles were determined using the Drop Analysis (LB-ADSA) plugin in ImageJ software (Figure 4).

3. Results and discussion

3.1 Surface morphology and topography evolution

The surface relief of 316L was examined using LSM with differential interference contrast imaging, showcasing surface roughness and 3D construction of the submicron-level surface topography in deformed 316L (Figure 5). Figure 5(a) shows the microstructure of the undeformed sample, presenting an almost flat surface with a slight relief, likely resulting from mechanical grinding. The evolution of surface relief in deformed 316L is shown in Figure 5(b-e) using DIC images. At 2%

strain (Figure 5(b)), the deformed surface exhibits annealing twins and relief morphology originating from slip lines. With increased strain, slip lines near grain boundaries develop in all grains, along with active slip lines on different slip systems. Figure 5(e) depicts multiple slip lines on the deformed surface after 25% strain. The visibility of these slip lines depends on the level of strain deformation, surface valleys, and peak heights. Compared to the undeformed 316L, the deformed sample shows a significantly smaller average grain size, and the increased presence of slip lines leads to surface morphological distortion. The area roughness parameter (Sa) was obtained from 3D laser microscopy, yielding Sa values of 0.062 μm for the undeformed sample and 0.350, 0.695, 1.017, and 1.667 μm for strains of 2%, 5%, 10%, and 25%, respectively. As noted, the Sa value characterizes the surface roughness at the submicron level. Based on the 3D surface topography, the surface at 25% strain is rougher than those at lower strain levels. Considering the roughness value (Sa), commercially available implants are classified into four groups: smooth (Sa = 0.5 mm), marginally rough (Sa = 0.5 mm to 1.0 mm), moderately rough (Sa = 1.0 mm to 2.0 mm), and rough (Sa > 2.0 mm) [6]. For 316L stainless steel bone plates, before and after deformation, all the samples investigated in this study fall into smooth or marginally rough categories. Surface roughness is an essential quantitative descriptor of topography, with alterations influencing the structural characteristics of the surface [7]. The surface topography of deformed 316L stainless steel was assessed using AFM, as illustrated in Figure 6. Figures 6(a-b) represent 10 μm × 10 μm scanning areas of the deformed samples with 2% and 5% strain, respectively. The 3D reconstructions of the atomic force micrographs exhibit topographic features with varying contrast levels, indicating an increase in the number of slip lines with rising strain. In Figure 6(c), the 10% strain sample reveals a higher concentration of slip lines than in the 2% and 5% strain samples. Slip intersections at grain boundaries, observed in Figure 6(d) corresponding to the 5% strain topography, are common occurrences. However, the topography of the 10% strain does not show slip lines intersecting grain boundaries. These findings suggest slip transfer (transfer of shear) during plastic deformation [4]. In summary, at 5% strain, slip lines converge at grain boundaries, while the topography at 10% strain indicates nonintersecting slip lines (Figures 6(d-e). Atomic force microscopy (AFM) is a powerful tool for examining the microstructure to identify and investigate slip intersections at grain boundaries under various strain levels. Detailed observations at 10% strain reveal significant changes in the deformation structure. Slip lines, which can appear linear or curved on the surface, exhibit notable alterations in orientation. Figure 6(a) illustrates these affected changes, highlighting the intersections of slip lines and providing insights into the complex deformation mechanisms at play.

Significant disparities in topographic height variations, reaching up to 400 nm at the grain boundary, are evident in Figure 6(f). The AFM image (20 μm × 20 μm scan size) shows a cross-sectional line profile and the corresponding height measurements. For medical implant applications, submicron topography plays a crucial role in bone bonding, while micron or coarse-micron topography is essential for the long-term interfacial stability of endosseous implants [8]. Surface observations made by AFM commonly use slip lines to gain insights into the motion of dislocations. With an increase in plastic strain, there is a concurrent increase in the concentration of dislocations within the grain interior. This leads to various intergranular dislocation–dislocation interaction processes associated with the glide of extended dislocations on different slip systems [9]. AFM observations can observe these characteristic features. Figure 6(g) shows slips activated across the surface of the 25% strained sample. Slip intersections act as precursors to martensite formation, as proposed by Olsen and Cohen [10]. This strain-induced martensitic transformation occurs at ambient temperature, signifying that martensite is formed at nucleation sites generated by plastic deformation, such as shear band intersections. To confirm the occurrence of martensitic transformation, the phase transformation of 316L can be evaluated morphologically at a microscopic level and through XRD analysis. XRD provides information about the crystallographic structure of martensite. In the context of surface observations by AFM, the development of slip bands provides information about plastic mechanisms, revealing the tendency of dislocations to move cooperatively in clusters on closely spaced slip planes or individually and independently. Observing slip steps at the surface [9,11] has been a valuable tool for understanding the cooperative motion of dislocations. The information collected at the surface is representative of the deformation within the bulk, aligning with observations from surface morphology analyses of deformed Cu [11]. A deformation twin at 10% strain, as shown in Figure 6(e), indicates an annealing twin characterized by the features of a twin boundary. The twin ribbon exhibits mirror characteristics of slip patterns across the twin boundary. S. Mishra *et al*. [12] have proposed that twin boundaries in deformed microstructures can have two possible origins: (1) the decay of original annealing twins and (2) the formation of deformation twins. The deformation process of 316L at different strain levels facilitates the identification of the relationship between relief morphology and the amount of deformation, predicting the degree of deformation that leads to relief features.

3.2 Phase identification

XRD profiles revealed the presence of austenitic and martensitic phases in 316L before and after deformation. Figure 7 shows the XRD profiles, with the primary phases appearing at 2θ approximately corresponding to the austenite, including γ(111), γ(200), γ(220), and γ(311). Figure 7(a) demonstrates asymmetric broadening at a diffraction angle of approximately 43°, with the deformed sample at 25% strain displaying the broadest peak width. In Figure 7(b), the α'-martensite (200) exhibits a weak reflection at a diffraction angle of 65°, and the intensities of diffraction peaks decrease with increasing deformation degree. Figure 7(c) confirmed the existence of ε-martensite which is in good agreement with previous study [4,15]. The XRD profile exhibits a broadening diffraction peak of α'-martensite (110) with increasing deformation. The broadening diffraction peaks indicate a decrease in average grain sizes, as observed in the LSM images. This slight increase in peak broadening and peak shifting can be attributed to the types of deformation mechanisms compared to the topographic characteristics.

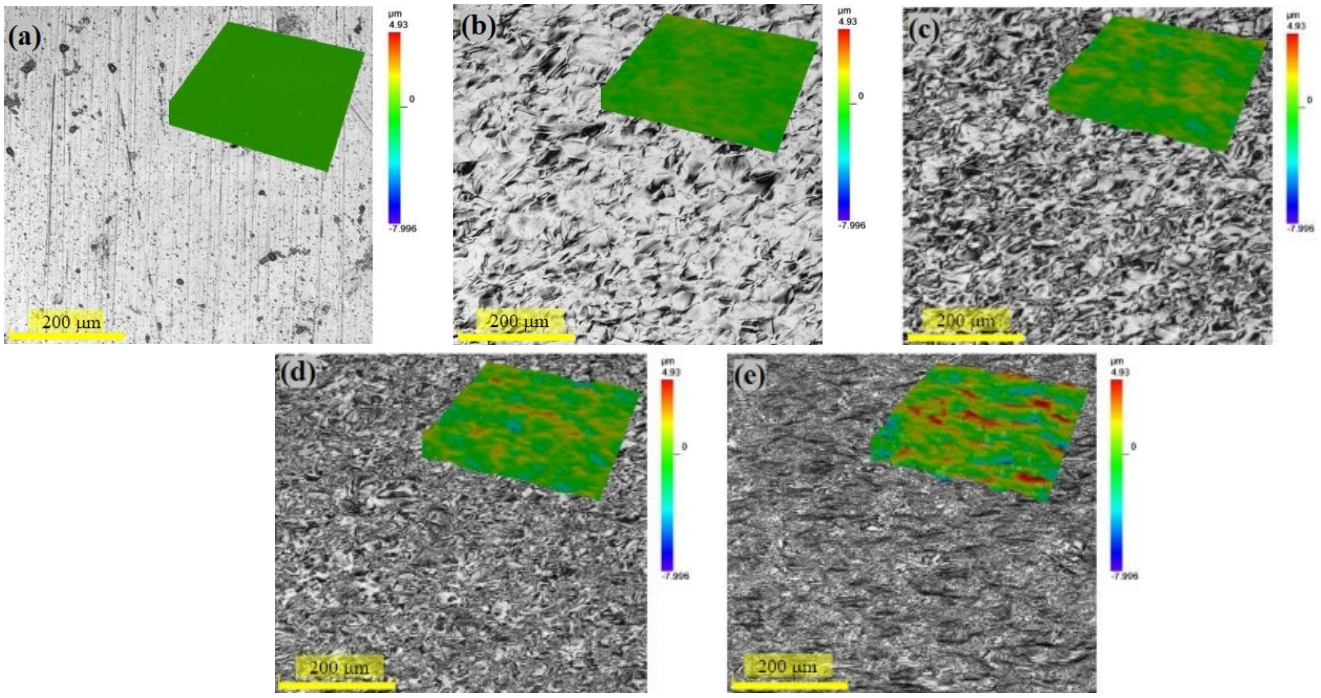

Figure 5. Laser scanning microscopy images and the inset of 3D surface topography of the 316L surface at various strain levels, (a) undeformed, (b) 2%, (c) 5%, (d) 10%, and (e) 25% strain.

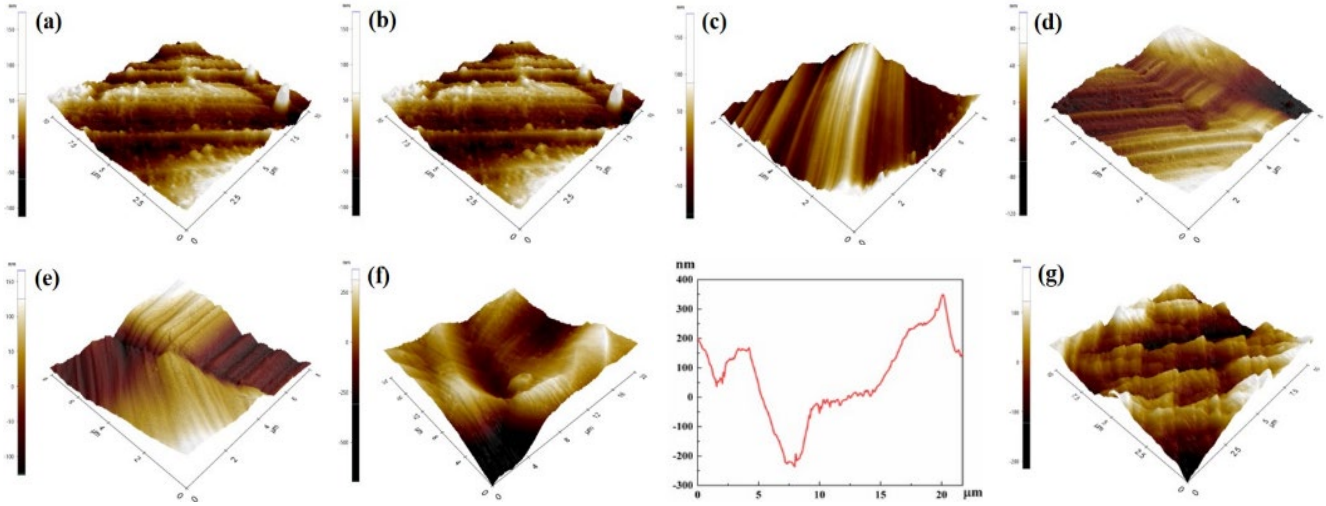

Figure 6. Evolution of surface relief in deformed samples at different strain levels, (a) 2%, (b) 5%, (c) 10%, (d) slip lines meet at grain boundary at 5%, (e) slip lines do not meet at grain boundary at 10%, (f) topographic height variations at 10%, and (g) slip intersections at 25% strain.

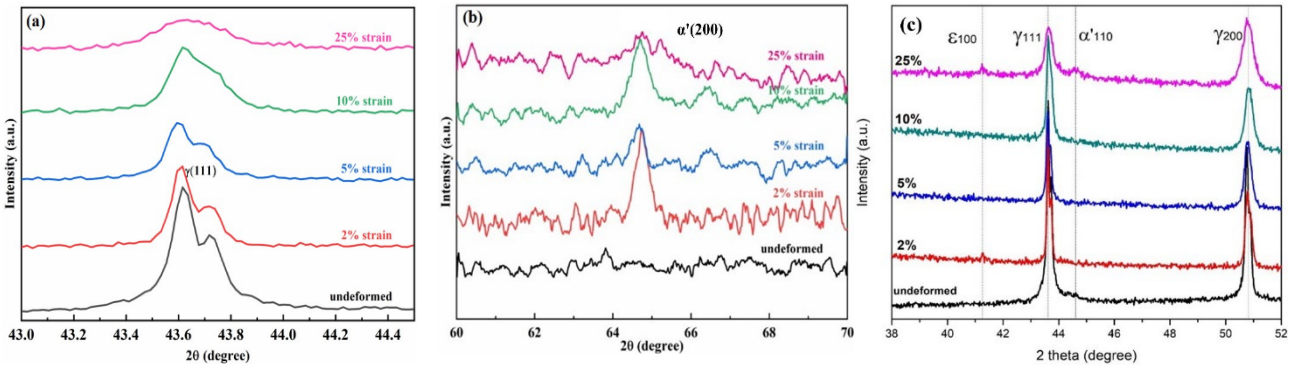

Figure 7. XRD profile utilized for phase identification on both the undeformed and deformed samples, (a) changes of austenite intensity, (b) at approximately of 65 degree shows α'(200) intensity with varying strain levels in 316L, and (c) the presence of ε-martensite.

The effect of roughness on the in vivo performance of metal implants has revealed both advantages and disadvantages. The corrosion properties of 316L are important and require careful consideration in material selection and the manufacturing process. Plastic deformation can damage the passive film on the surface because microstructural changes during plastic deformation typically involve martensitic transformation, twinning, and slip. In the case of metallic medical implants, the topmost atomic layer of the surface comes into contact with fluids, and the passive layer provides corrosion protection. However, it is not impervious to plastic deformation, potentially leading to allergenicity. The nickel content in stainless steel may serve as the cancer-causing element that could be released into the body during corrosion [13,14].

3.3 Contact angle measurements and surface free energy calculation

The contact angle measurements of multiple liquid droplets on 316L surfaces revealed different wetting properties. The level of deformation affected the functional wettability of the 316L surface. Figure 8 shows similar trends for two different liquids, with contact angle values decreasing as the percent strain increased. These findings align well with the observed topographical changes in the LSM micrographs (Figure 5), indicating a significant effect of surface characteristics, such as surface topography and roughness, on the wettability of 316L. The contact angle increases with the average surface roughness (Sa).

The calculated surface free energy was determined from the Owens–Wendt relationship by comparing the contact angles of water and glycerol on the surfaces. Figure 9 shows the Owens–Wendt relationship between water and glycerol on 316L surfaces processed at various degrees of deformation. As the degree of deformation increases, the surface roughness of 316L also rises, leading to enhanced surface free energy values. However, the surface free energy of the deformed sample after 2% strain (Figure 10) was lower than that of the undeformed sample. This suggests the presence of key factors influencing surface free energy. Ye Tian *et al.* [4] described that ε-martensite introduces the nucleation of α′-martensite and facilitates its formation at individual shear bands. With increasing surface free energy and the prevalence of deformation twins, slip intersections become dominant nucleation sites for α'-martensite. In our study, the surface free energy decreased from 6.75 $mN{\cdot}m^{-1}$ to 4.37 $mN{\cdot}m^{-1}$ for the undeformed and 2% strain-deformed samples, aligning with the XRD results that identified α' martensite phases in the deformed sample. Our findings align with an electron backscatter diffraction study on SUS321 stainless steel microstructural evolution under different strains during deformation-induced martensitic transformation (DIM). The study observed that ε-martensite was likely initiated within the slip band, challenging the previously assumed classical initiation theory at slip band intersections. Slip bands were identified as the preferred nucleation sites [15]. Volume expansion occurred owing to the sudden reorientation of C and Fe atoms during martensitic transformation [16]. Decreased surface free energy drives the nanoscale lattice reorientation [17,18]. The plastic deformation influences the formation of the passive layer owing to the presence of oxide. The outer layer comprises Fe(III) oxide, while the inner layer comprises Cr(III) oxide on the steel surface [19]. A study on the influence of plastic deformation on 304 stainless steel passive film reported changes in elemental composition content owing to the oxide passive surface film and deformation-induced martensite introduction through cold rolling [20]. Results revealed that the oxide content decreased if the α′ phase was less than 6%. Furthermore, after deformation under 10% strain, the polar and dispersive components of the estimated surface free energy values decreased, indicating a reduction in the surface free energy of the 316L surface.

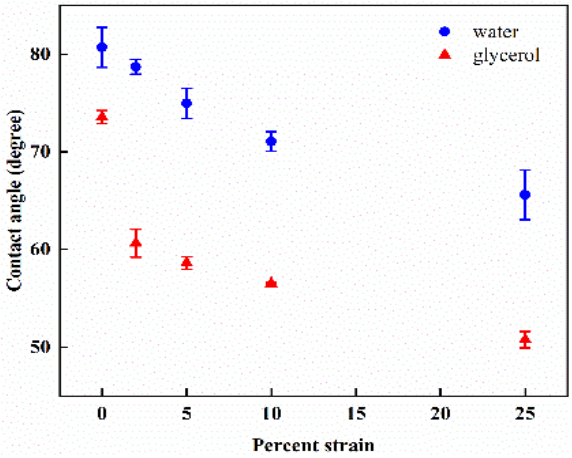

Figure 8. Average contact angles of water (blue circles) and glycerol (red triangles).

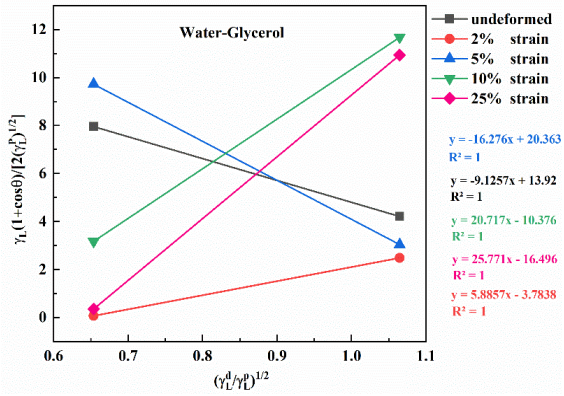

Figure 9. Owens–Wendt profile based on the contact angles of water and glycerol.

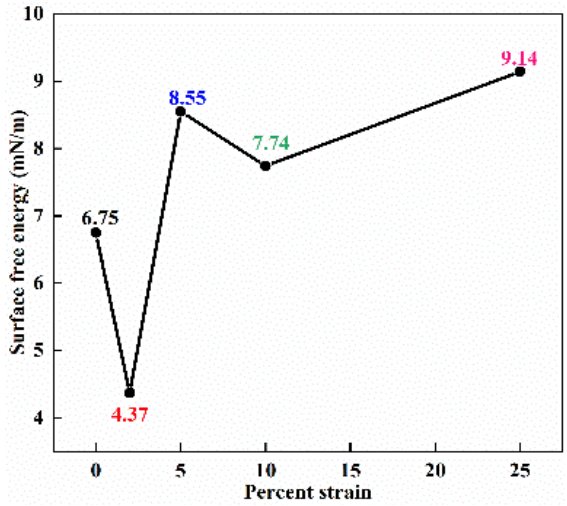

Figure 10. Surface free energy of the 316L surface at various strain levels.

The rise in surface free energy was ascribed to the plastic deformation behavior, a phenomenon explored by numerous researchers. Henry Bueno [21] clarified that the total surface tension of the solid was influenced by surface characteristics such as relief and crystallographic orientation. Peaks and valleys on a surface contribute to an increased surface area as roughness increases. A similar study highlighted that deformation features significantly change surface topography and increase surface roughness [22]. This increase in surface free energy was linked to plastic deformation behavior. At elevated levels of strain, particularly at higher degrees, the intensity of the γ-austenite peak decreases.

4. Conclusions

The evolution of the deformed surfaces in 316L stainless steel correlates with the strain variation. Comparing the topographical features observed in AFM with the phases detected by XRD measurement enables the identification of deformation mechanisms and the sequence of the DIM transformation, $\gamma \rightarrow$ slip lines $\rightarrow \alpha'$, during tensile deformation. Results from contact angle measurement and surface free energy determination indicate a higher degree of wettability after plastic deformation. However, the observed DIM transformation on the surface may damage the passive film, resulting in corrosion and a reduced implant lifespan. Notably, the 10% strain sample showed a decrease in surface free energy. In bioimplant applications, deformed surfaces are found characterized by a mean roughness falls falling within the 0.062 μm to 1.667 μm range.

Acknowledgment

K. Antanam acknowledges Suranaree University of Technology for financial support through the Honorary Graduate Scholarship Program.

References

[1] S. Wu, S. Altenried, A. Zogg, F. Zuber, K. Maniura-Weber, and Q. Ren, "Role of the surface nanoscale roughness of stainless steel on bacterial adhesion and microcolony formation," *ACS omega*, vol. 3, no. 6. pp. 6456-6464, 2018.

[2] L. Susanna, "Surface free energy – what is it and how to measure it?," Biolin Scientific.com. https://www.biolinscientific.com/blog/how-to-measure-surface-free-energy (accessed Apr. 6, 2020).

[3] S. Cicek, A. Karaca, I. Torun, M.S. Onses, and B. Uzer, "The relationship of surface roughness and wettability of 316L stainless steel implants with plastic deformation mechanisms," *Materials Today: Proceedings*, vol. 7, pp. 389-393, 2019.

[4] Y. Tian, O. I. Gorbatov, A. Borgenstam, A. V. Ruban, and P. Hedström, "Deformation microstructure and deformation induced martensite in austenitic Fe-Cr-Ni alloys depending on stacking fault energy," *Metallurgical and materials transactions A*, vol. 48, no. 1, pp. 1-7, 2017.

[5] Z. Zhang, W. Wang, A. N. Korpacz, C. Dufour, Z. J. Weiland, C. R. Lambert, and M. Timko, "Binary liquid mixture contact-angle measurements for precise estimation of surface free energy," *Langmuir*, vol. 35, no. 38, pp. 12317-12325, 2019.

[6] A. M, O. Omar, W. Xia, and A. Palmquist, "Dental Implant surfaces – physicochemical properties, biological performance and trends implant dentistry," *Implant Dentistry-A Rapidly Evolving Practice*, vol. 1, pp.19-56, 2011.

[7] A. Shenoy, "The effect of surface roughness on the fretting corrosion of 316L stainless steel biomaterial surfaces," PhD diss., Syracuse University, 2014.

[8] J. E. Davies, E. Ajami, R. Moineddin, and V. C. Mendes, "The roles of different scale ranges of surface implant topography on the stability of the bone/implant interface," *Biomaterials*, vol. 34, no. 14, pp. 3535-3546, 2013.

[9] J. P. Hirth, and L. Kubin, "Cross-slip," in Handbook of Dislocations in solids, 2009, pp. 15-17.

[10] P Hedström, "Deformation and martensitic phase transformation in stainless steels," Ph.D. dissertation, Luleå tekniska universitet, 2007.

[11] M. Montagnat, J. Weiss, J. Chevy, P. Dubal, H. Brunjail, P. Bastie, and J. G. Sevillano, "The heterogeneous nature of slip in ice single crystals deformed under torsion," *Philosophical Magazine*, vol. 86, no. 27, pp. 4259-4270, 2006.

[12] S. Mishra, K. Narasimhan, and I. Samajdar, "Deformation twinning in AISI 316L austenitic stainless steel: role of strain and strain path," *Materials Science and Technology*, vol. 23, no. 9, pp. 1118-1126, 2007.

[13] N. Eliaz, "Corrosion of metallic biomaterials: A review," *Materials*, vol. 12, no. 3, p.407, 2019.

[14] A. Nouri, and C. Wen, "Introduction to surface coating and modification for metallic biomaterials," *Surface Coating and Modification of Metallic Biomaterials*, pp. 3-60, 2015.

[15] J. L. Wang, M. H. Huang, X. H. Xi, C. C. Wang, and W. Xu, "Characteristics of nucleation and transformation sequence in deformation-induced martensitic transformation," *Materials Characterization*, vol. 163, p. 110234, 2020.

[16] N. Solomon, and I. Solomon, "Phase transformation influence on corrosion resistance of AISI 316 austenitic stainless steel," *UPB Scientific Bulletin*, vol. 72, pp. 197-207, 2010.

[17] F. Ma, K. W. Xu, and P. K. Chu, "Surface-induced structural transformation in nanowires," *Materials Science and Engineering*, vol. 74, no. 6, pp. 173-209, 2013.

[18] Q. Zu, Y. F. Guo, and X. Yao, "Surface and orientation effects on stress-induced hcp-fcc phase transformation in Ti nanopillars," *Applied Surface Science*, vol. 509, p. 145234, 2020.

[19] Z. Wang, F. Di-Franco, A. Seyeux, S. Zanna, V. Maurice, and P. Marcus, "Passivation-induced physicochemical alterations of the native surface oxide film on 316L austenitic stainless steel," *Journal of The Electrochemical Society*, vol. 166, no. 11, pp. C3376-C3388, 2019.

[20] S. He, D. Jiang, and Z. Sun, "Effect of deformation-induced martensite on protective performance of passive film on 304 stainless steel," *International Journal of Electrochemical Science*, vol. 13, no. 5, pp. 4700-4719, 2018.

[21] H. Bueno, "The critical surface tension of 316L stainless steel," M.S. Thesis, San Jose State University, 2005.

[22] B. Uzer, "Modulating the surface properties of metallic implants and the response of breast cancer cells by surface relief induced via bulk plastic deformation," *Frontiers in Materials*, vol. 7, p. 99, 2020.